

Channel Measurements and Modeling for Dynamic Vehicular ISAC Scenarios at 28 GHz

Zhengyu Zhang, *Student Member, IEEE*, Ruisi He, *Senior Member, IEEE*, Bo Ai, *Fellow, IEEE*,
Mi Yang, *Member, IEEE*, Xuejian Zhang, Ziyi Qi and Yuan Yuan

Abstract—Integrated sensing and communication (ISAC) is a promising technology for 6G, with the goal of providing end-to-end information processing and inherent perception capabilities for future communication systems. Within ISAC emerging application scenarios, vehicular ISAC technologies have the potential to enhance traffic efficiency and safety through integration of communication and synchronized perception abilities. To establish a foundational theoretical support for vehicular ISAC system design and standardization, it is necessary to conduct channel measurements, and modeling to obtain a deep understanding of the radio propagation. In this paper, a dynamic statistical channel model is proposed for vehicular ISAC scenarios, incorporating Sensing Multipath Components (S-MPCs) and Clutter Multipath Components (C-MPCs), which are identified by the proposed tracking algorithm. Based on actual vehicular ISAC channel measurements at 28 GHz, time-varying sensing characteristics in front, left, and right directions are investigated. To model the dynamic evolution process of channel, number of new S-MPCs, lifetimes, initial power and delay positions, dynamic variations within their lifetimes, clustering, power decay, and fading of C-MPCs are statistically characterized. Finally, the paper provides implementation of dynamic vehicular ISAC model and validates it by comparing key simulation statistics between measurements and simulations.

Index Terms—Integrated sensing and communication (ISAC), Vehicular channel measurement, Dynamic statistical channel model, Millimeter waves.

I. INTRODUCTION

With the development of wireless communication systems, the sixth generation (6G) network not only represents an enhancement of current communication technologies, but also possesses the capability to provide ubiquitous sensing, seamless connectivity and advanced intelligence through wireless devices [1]. In this vision, higher demands for end-to-end information processing ability and native perception ability of 6G networks are required, so as to prompt the recent research interest in integrated sensing and communication (ISAC) techniques [2]. Technically, ISAC can enhance spectrum and energy efficiency while reducing hardware and signal processing costs, which is achieved by enabling the integration of sensing and communication functionalities within a single transmission, device, or network infrastructure [3]. ISAC has been expected to enable communication-assisted sensing or sensing-assisted communication, which enhances

jointly sensing and communication applications in 6G scenarios, including smart home systems, enhanced positioning and tracking, human-computer interaction, environmental monitoring, sensing-assisted beam training, and so on [4].

Recently, ISAC techniques have emerged as a pivotal component in the vehicle industry, playing a crucial role in enhancing vehicle safety and performance [5]–[7]. Under the background of deep integration of communication and sensing technologies in the vehicle industry, vehicular ISAC networks is one of the most potential ISAC application scenarios. On the one hand, lots of communication transceivers and sensors are equipped on the autonomous vehicles [8]. For example, the novel vehicles is usually equipped with eight cameras for a 360-degree of environment perception [9]. On the other hand, for vehicular ISAC, it is possible to reuse the current dense deployment road-side units (RSUs) for sensing with only minor modifications in hardware, signaling strategy, and communication standards [10]–[12]. In this way, vehicular ISAC can connect vehicles with surrounding vehicles, traffic infrastructures, and networks, as well as use the integration gain of ISAC to obtain more accurate perception information and better wireless communication quality, so as to reduce traffic jams and accident rates efficiently.

However, vehicular ISAC technologies are in its early stages, and a deep understanding of the radio propagation mechanism of wireless channel is crucial for its design, performance evaluation, and standardization [13]–[15]. In contrast to traditional communication channels, vehicular ISAC channels integrate both sensing and communication channels. This integration encompasses radio propagation from the communication transmitter to the communication receiver, as well as echo propagation from the sensing transceiver to scatterers and back to the sensing transceiver [16], [17]. Therefore, vehicular ISAC channels are more sensitive to the driving environment, such as surrounding vehicles, people and other scatterers. This leads to the presence of abundant effective sensing multipaths as well as clutters, with a more rapid birth and death process for them. Moreover, owing to the dynamics of these scatterers and the mobility of vehicles, time-varying behavior is a crucial characteristic of vehicular ISAC channels, which should be sufficiently incorporated into channel modeling. Besides, during the driving process of vehicles, the road conditions and environmental distributions vary across different sensing directions, such as the types of scatterers, time-varying behavior, etc., resulting in distinct channel characteristics, it is necessary for different directions to model vehicular ISAC channels accordingly.

Zhengyu Zhang, Ruisi He, Bo Ai, Mi Yang, Xuejian Zhang, Ziyi Qi and Yuan Yuan are with the School of Electronics and Information Engineering, Beijing Jiaotong University, Beijing 100044, China.

Therefore, dynamic vehicular ISAC channel modeling is a challenging task, the professional channel measurements and characterization are necessary for accurate modeling [18]. Over the past few years, extensive research has been conducted on vehicular channel measurements and models, with a predominant focus on communication channels where transmitters and receivers are mounted in different positions, and these studies are mostly conducted in sub-6 GHz frequencies rather than millimeter waves, which are more attractive for ISAC technologies. For example, Ref. [19] presented a MIMO model for Vehicle-to-Vehicle (V2V) channels based on measurements performed at 5.2 GHz in highway and rural environments. An extensive communication channel measurements are conducted in a straight subway tunnel at 1.8 and 5.8 GHz in Ref. [20] and on a suspension bridge and a beam bridge at 5.9 GHz in Ref. [21], respectively. Measurement results and propagation channel model are presented in Ref. [22], in which a bus acts either as a shadowing object or as a relay between two passenger cars. Dynamic time-varying has been main characteristics in vehicular channels. Ref. [23] carried out measurement campaigns and analyzed the non-stationarity of V2V channels as well as vehicle-to-infrastructure (V2I) channels. Ref. [24] proposed a dynamic wideband directional channel model based on measurements conducted at 5.3 GHz in suburban, urban, and underground parking environments. By incorporating dynamic behaviors of the MPCs, the model is capable of handling time-varying characteristics. In Ref. [25], channel measurements at 5.9 GHz in street intersection scenarios are carried out and provide data for the characterization and modeling of time-varying vehicular channels. Ref. [26] proposed a geometric MIMO channel model, which is adaptable to a variety of millimeter-wave mobile-to-mobile scenarios. Although the aforementioned vehicular channel measurements covers most dynamic scenarios, these measurements and models cannot be generalized to vehicular ISAC channels.

On the other hand, the literature on ISAC channel measurements and models is relatively scarce and mainly focuses on non-dynamic scenarios, resulting in a lack of time-varying characteristics. Ref. [27] analyze the ISAC channel characteristics based on the measurements at 28 GHz in an outdoor scenario, where a metal board is placed in a stationary position as sensing target. Ref. [28] compared ISAC channel characteristics between communication channels and sensing channels through actual measurements in outdoor static scenarios, and the correlation model of multipaths in ISAC channels are measured and characterized in Ref. [29]. Ref. [30] measured the azimuth power spectrum of vehicular ISAC channels, while the vehicles are moving slowly due to narrow experimental space. Ref. [31] conducted communication and sensing channel measurements for an indoor static scenario at 28 GHz. These static measurement scenarios cannot reflect the time-varying characteristics of ISAC channels. Besides, ISAC channel models for various application scenarios have also been widely researched. In Ref. [32], a vehicle ISAC system based on IEEE 802.11ad is presented, where communication channel is considered as a Rice channel and sensing channel is considered as a path-based model. Ref. [33] proposed a

scatterer-based hybrid channel model framework, which first generate scatterers in the propagation environment and then use simplified ray-tracing to generate channels. In Ref. [34], a novel ISAC channel model combining forward and backward scattering is proposed, where the correlations are investigated. In Ref. [35], a unified approach to model an ISAC channel is proposed, where the pathloss, LOS probability, Doppler and the fast fading are provided systematically. However, similar to ISAC channel measurements, these models is difficult to represent dynamic evolution over time, such as the lifetimes of multipaths, making them unsuitable for application in vehicular ISAC scenarios. To the best of the authors' knowledge, there exist few actual channel measurements and modeling for dynamic vehicular ISAC scenarios.

As mentioned earlier, despite numerous efforts in measuring and modeling of vehicular channels, these studies have primarily focused on communication channels, lacking a comprehensive representation of the characteristics of sensing channels, especially their dynamic characteristics. To fill the gap, this paper conducts vehicular channel measurements from the perspective of sensing and proposes a measurement-based dynamic statistical channel model aiming for vehicular ISAC scenarios. The main contributions are summarized as

- 1) A novel dynamic ISAC channel tapped-delay line model is proposed. In the proposed model, multipaths are categorized into two groups: sensing multipath components (S-MPCs) and clutter multipath components (C-MPCs), each described with its own statistical distribution.
- 2) A vehicular ISAC channel measurement system is used to conduct dynamic channel measurements at 28 GHz in different directions, including front, left and right directions. The transmitter and receiver both mounted on a vehicle to focus on the time-varying sensing characteristics.
- 3) A tracking algorithm is utilized to identify S-MPCs and C-MPCs, and a series of characterization, including number of new S-MPCs, lifetimes, initial power and delay positions, dynamic variations within their lifetimes, clustering, power decay and fading of C-MPCs, is statistically modeled to enable simulated channel with dynamic evolution process.
- 4) Comparisons of channel characteristic parameters between measurements and simulations are conducted to implement and validate the model, which reflect the accuracy and effectiveness of the proposed model.

The remainder of this paper is structured as follows. In section II, a dynamic channel model is proposed for vehicular ISAC scenarios. Section III introduces the vehicular ISAC channel measurement system and measurement campaign. In section IV, the data processing for modeling are presented, including S-MPCs and C-MPCs modeling. Section V presents the channel model implementation and validation. Finally, the conclusion is given in Section VI.

II. DYNAMIC ISAC CHANNEL MODEL

To model vehicular ISAC channels with time-varying characteristics, we introduce a novel dynamic ISAC channel

tapped-delay line model in this paper, which is composed of S-MPCs and C-MPCs. For S-MPCs, they typically exhibit higher power and more pronounced clustering, attributed to the strong reflection from sensing targets, and occur continuously over time. In contrast, C-MPCs have lower power and are generally distributed across the entire delay domain due to widespread scatterers and noise, and occur randomly over time. The ISAC channel impulse response can be expressed as

$$h(t, \tau) = \sum_{l=1}^{L(t)} a_l(t) e^{j\varphi_l} \cdot \delta(\tau - \tau_l(t)) + \sum_{n=1}^{N(t)} a_n(t) e^{j\varphi_n} \cdot \delta(\tau - \tau_n(t)) \quad (1)$$

where $\delta(\cdot)$ is the Dirac delta function, $L(t)$ is the number of effective S-MPCs, $N(t)$ is the number of C-MPCs, $a_l(t)$, $\tau_l(t)$ as well as $a_n(t)$, $\tau_n(t)$ are the amplitude and delay of the l th and n th MPCs at time t respectively. Noted that $a_l(t)$, $\tau_l(t)$ and $a_n(t)$, $\tau_n(t)$ are time-varying parameters. φ_l and φ_n are the phase and are assumed to be uniformly distributed in the range of $[0, 2\pi]$.

For time-varying vehicular ISAC channels, the behavior of S-MPCs changes continuously over time, while C-MPCs remain time-varying and independent at each time. Specifically, due to vehicular movement and dynamic scatterers, each S-MPC has own lifetime that appear and disappear at random time instant, and the amplitude and delay are time-varying within lifetimes. Due to random and unknown environment, C-MPCs are modeled as a type of random distribution characterized by specific statistical properties. The set of all S-MPCs that exist at time instant t_i are L_i , which consist of two sets of S-MPCs, as follows:

$$L_i = L_{1,i} \cup L_{2,i} \cup \dots, L_{j,i} \cup \dots, L_{i-1,i} \cup L_{i,i} \quad (2)$$

where $L_{i,i}$ is the set of S-MPCs that first appear at time t_i , and $L_{j,i}$ is the set of S-MPCs that first appear at time t_j and still exist at time t_i . The indexes of path in $L_{i,i}$ and $L_{j,i}$ are $l_{i,i} = 1, 2, \dots, N(t_{i,i})$ and $l_{j,i} = 1, 2, \dots, N(t_{j,i})$ respectively. And the number of all effective S-MPCs at time t_i is expressed as

$$L(t_i) = L(t_{i,i}) + \sum_{j=1}^{i-1} L(t_{j,i}) \quad (0 < j < i) \quad (3)$$

The channel impulse response at time t_i can be reconstructed based on the collection of S-MPCs in all sets of $L_{i,i}$ and $L_{j,i}$, as well as C-MPCs across all delay bins. Considering the time-varying characteristics, channel impulse response can be thus expressed as

$$h(t_i, \tau(t_i)) = \sum_{j=1}^{i-1} \sum_{l_{j,i}=1}^{L(t_{j,i})} a_{l_{j,i}}(t_i) e^{j\varphi_{l_{j,i}}} \cdot \delta(\tau - \tau_{l_{j,i}}(t_i)) + \sum_{l_{i,i}=1}^{L(t_{i,i})} a_{l_{i,i}}(t_i) e^{j\varphi_{l_{i,i}}} \cdot \delta(\tau - \tau_{l_{i,i}}(t_i)) + a(t_i, \tau(t_i)) e^{j\varphi} \quad (4)$$

The first term of equation (4) represents the old S-MPCs that appeared before time t_i , the second term of equation (4) represents the new S-MPCs that appeared at time t_i , and the third term of equation (4) represents the immediate C-MPCs that existed at time t_i and delay $\tau(t_i)$. By modeling the ‘‘birth’’ and ‘‘death’’ processes of S-MPCs and the clutter floor of C-MPCs, the channel model can generate the dynamic and successive evolutions of impulse response at any time. In order to provide the proposed model, we statistically extract the following parameters from measurements:

- the length of S-MPCs lifetime;
- the number of newly appearing S-MPCs in each snapshot;
- the initial power and delay of newly appearing S-MPCs in each snapshot;
- the dynamic evolution of power and delay of S-MPCs over successive snapshots within the lifetime;
- the clustering of S-MPCs in each snapshot;
- the power decay and small-scale fading of C-MPCs in each snapshot.

Utilizing the statistical characterization of the aforementioned parameters, a dynamic ISAC channel model can be developed to simulate time-varying channels.

III. MEASUREMENT CAMPAIGN

A. Measurement System

The vehicular ISAC channel measurement system is designed as shown in Fig. 1, including a signal generator based transmitter (TX), a signal digitizer based receiver (RX), and a power supply based on the vehicular battery. The architecture and key equipment of measurement system are illustrated in Fig. 1 and Fig. 2 respectively. For TX, the National Instruments (NI) PXIe-5745 is employed as ‘‘signal generator’’, which generates the baseband signals with 1 GHz bandwidth. Then, baseband signals are converted to 28 GHz frequency through the up-conversion module, and transmitted through a power amplifier with gain of 28 dB and horn antennas with a directional beamwidth of 15 degrees and gain of 20 dB. For RX, sounding signals are received through array antennas and electronic switches. The array antenna is a 32-element rectangular array with gain of 5 dB, and different channels in the switches are utilized to enhance received signals. Then, they are converted to baseband through the down-conversion module and stored. During the measurement, RGB video data from the camera and point-cloud data from the radar are collected and stored simultaneously to aid in mapping between channel MPCs and environmental scatterers. The TX and RX are synchronized by the rubidium clocks and Global Navigation Satellite System (GNSS) antennas, which can provide 10 MHz reference clock as well as vehicle’s position. The inverter is employed to convert the vehicular 12V DC battery to 220V AC, and uninterruptible power supplies (UPS) is employed to provide stable power to the measurement equipment. The detailed configurations of vehicular ISAC channel measurement system are presented in Table I. Prior to measurements, back-to-back measurements are conducted to eliminate the impact of measurement equipment, such as cables, switches, transceivers, etc, thereby ensuring accurate measurement data.

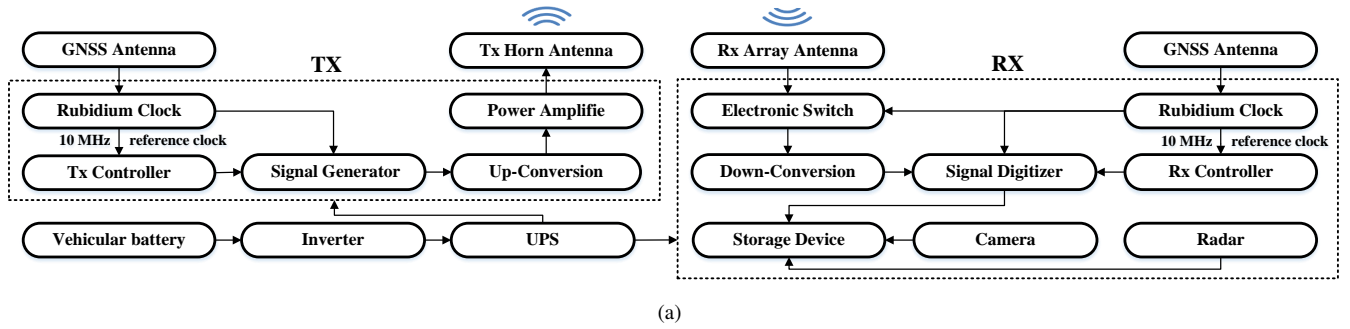


Fig. 1. Vehicular ISAC channel measurement system.

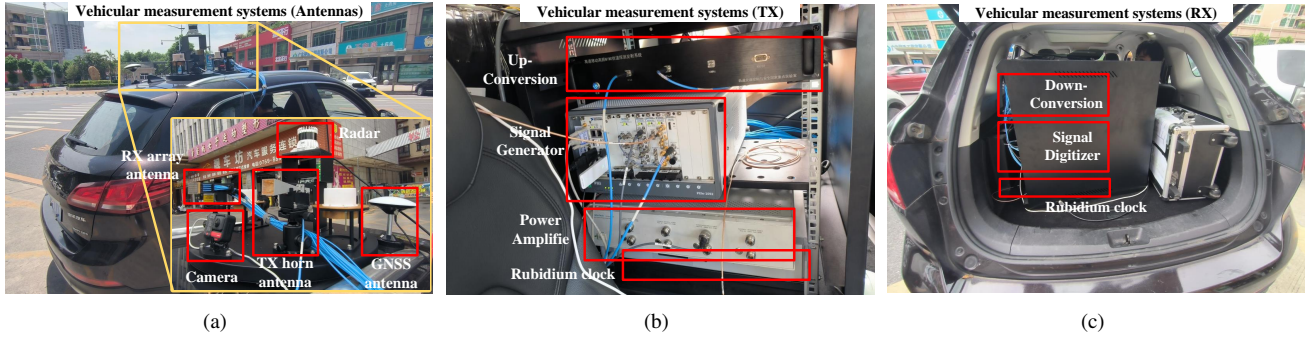


Fig. 2. Key equipment of vehicular ISAC channel measurement system. (a) Antennas. (b) TX. (c) RX.

TABLE I
CONFIGURATIONS OF ISAC MEASUREMENT SYSTEM.

Parameters	Value
Center frequency	28 GHz
Bandwidth	1 GHz
Transmit power	28 dBm
Delay resolution	1 ns
Sounding signal	Multi-carrier signal
Transmitter antenna	Horn antenna
Receiver antenna	4×8 array antenna
Vehicle speed	30 km/h
Transceiver height	2.3m

B. Measurement Scenarios

The measurements were conducted in the Songshanhu district of Dongguan, located in Guangdong, China. The red line in Fig.3 (a) shows the trajectory diagram of vehicles for a single measurement route. The mean vehicle speed is 30 km/h and duration of measurements is generally between 20 and 25 minutes. From the satellite photographs in Fig. 3 (a), the measured streets are surrounded by buildings, trees, shrubs, etc., exhibiting varying environmental characteristics in different sensing directions. The sensing directions during the measurements are shown in Fig.3 (b), including front, left and right directions. The camera view from different directions are shown as Fig.3 (c)-(e). It is obvious that different directions have their own primary scatterers, leading to distinct environmental characteristics as follows:

- *Front*: The main sensing scatterers include traffic lights in front of RX and preceding vehicles. Due to the forward

extension of the road, the behavior of scatterers is mainly observed as being close to or far from the transceiver, resulting in a large dynamic range of distances for these scatterers from the transceiver. Besides, due to the high-speed movement, there aren't always sensing scatterers present in the front during the measurements.

- *Left*: The main sensing scatterers include the median barriers, vehicles on the opposite road, and distant buildings. Due to the rapid movement of vehicles, these scatterers are often only perceptible for a short period of time. Besides, due to the distribution of these scatterers along the road, there are noticeable sensing scatterers for the majority of the measurement time.

- *Right*: The main sensing scatterers include vehicles on the same-direction road and nearby buildings. Similar to the left direction, these scatterers often appear for only a short period of time. However, due to being on the same side of the road, vehicles traveling in the same direction may be perceptible for a longer duration. Additionally, the S-MPCs contributed by nearby buildings have higher powers than left.

Therefore, we statistically model the three main sensing directions separately in this paper, obtaining directional ISAC channel models.

IV. DATA PROCESSING

A. Power Delay Profile

During the measurements, due to the long driving route, unavoidable situations include waiting for traffic red lights. Therefore, prior to data processing, we eliminate intervals where the vehicle is static for waiting at traffic lights, based

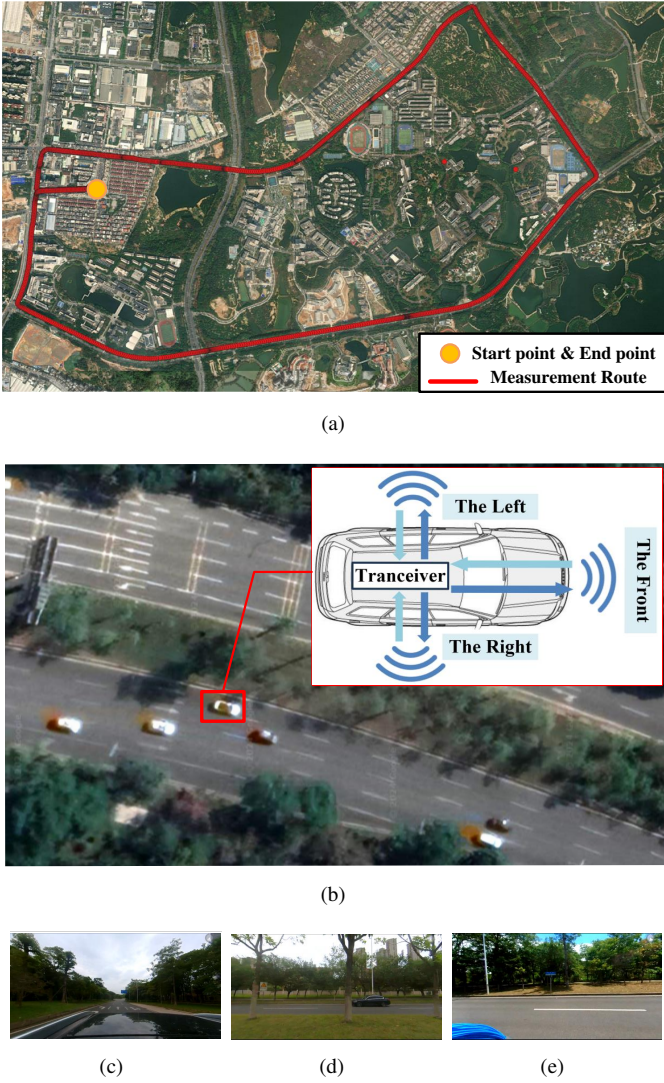


Fig. 3. Measurement scenarios. (a) Measurement route and satellite photographs. (b) Sensing directions during the measurements. (c) Camera view from the front. (d) Camera view from the left. (e) Camera view from the right.

on synchronized video data, ensuring the continuous dynamics of the channel. Power delay profiles (PDPs) are widely used to reflect the received paths with propagation delays, which is calculated as follows:

$$PDP(t, \tau) = |h(t, \tau)|^2 \quad (5)$$

The PDPs of different directions are shown in fig. 4, which have different dynamic channel characteristics. It can be observed that the power in the left or right directions is higher than that in the front directions. This is attributed to scatterers, such as trees and buildings along the road, which result in strong and continuous echo signals, leading to higher energy in the left or right directions when the vehicle is in motion. Furthermore, the diversity of multipath in the left or right direction is significantly greater than that in the front directions, and tend to occur at low delays and span across a wider range in the time domain. Besides, for the front direction, multipaths exhibit sparsity in the time domain and a wider range of delays, which is attributed to the larger

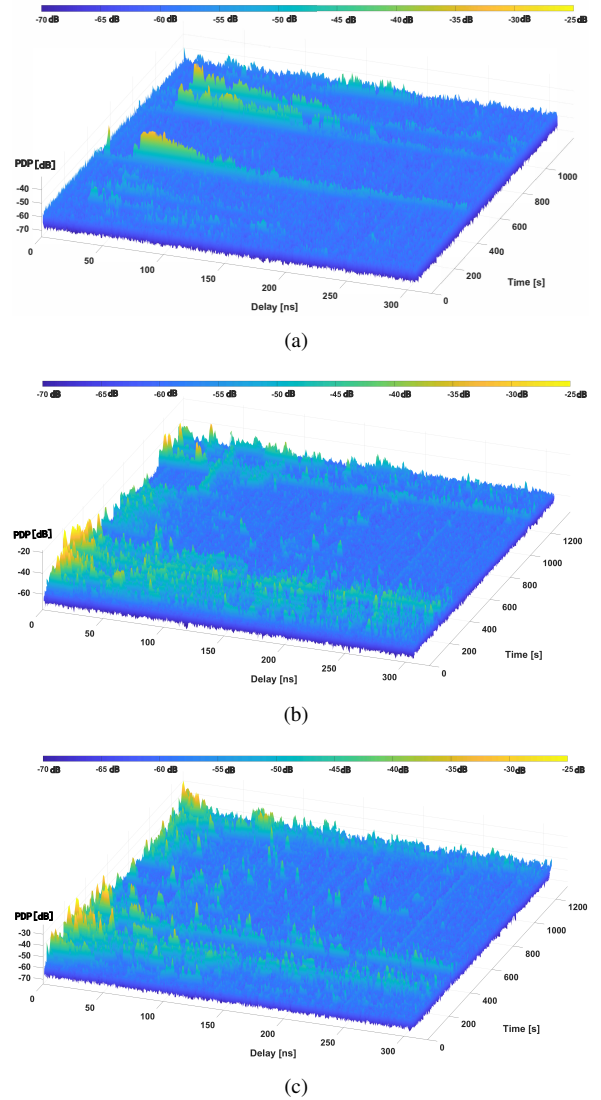


Fig. 4. Dynamic PDPs of vehicular ISAC channels in different directions. (a) Front. (b) Left. (c) Right.

spatial depth of perceived targets, such as preceding vehicles, and there is a gap at low delays, which can be attributed to maintaining a safe driving distance.

To distinguish between S-MPCs and C-MPCs, we apply a sensing threshold for the initial preprocessing of measured PDPs, as illustrated in Fig. 5. The sensing threshold in this paper is set to be 6 dB above the noise floor. The S-MPCs have more power and are effective and positive for sensing, while C-MPCs lack sufficient power to be perceived and are usually submerged in noise.

B. S-MPCs Modeling

1) *S-MPC Tracking*: In practice, it is possible that the powers of some sudden clutters are higher than sensing threshold. Therefore, relying only on the sensing threshold is insufficient for extracting S-MPCs. Compared to C-MPCs, S-MPCs occur continuously over time. Thus, we use a MPC distance (MCD)-based tracking algorithm to extract S-MPCs more accurately and reasonably. MCD is used to measure the

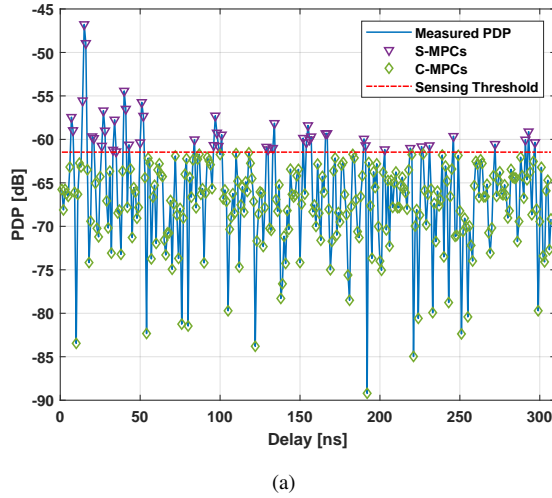


Fig. 5. Distribution of S-MPCs and C-MPCs based on sensing threshold.

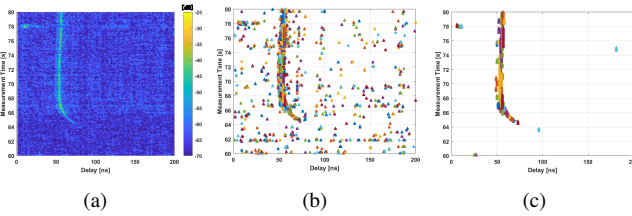


Fig. 6. S-MPC tracking results. (a) Raw PDPs. (b) After sensing threshold. (c) After filtering and handover.

distance between two MPCs, where a smaller MCD indicates a higher degree of similarity between two MPCs. A heuristic normalized amplitude factor is introduced to enhance accuracy [19], and the calculation for MPCs l_1 and l_2 is as follows:

$$MCD = \left(\frac{1}{\Delta a_{\max}} \right) \left| \frac{a_1(t_i)}{a_2(t_{i+1})} \right| \cdot \frac{\tau_{std}}{(\Delta \tau_{\max})^2} \cdot |\tau_1(t_i) - \tau_2(t_{i+1})| \quad (6)$$

where

$$\Delta \tau_{\max} = \max(\tau_l) - \min(\tau_l) \quad (7)$$

$$\Delta a_{\max} = \frac{\max(a_l)}{\min(a_l)} \quad (8)$$

and a_1 and a_2 are amplitudes of MPCs l_1 and l_2 respectively, τ_1 and τ_2 are delays of MPCs l_1 and l_2 respectively, a_l , τ_l and τ_{std} are amplitudes, delays and a standard deviation of delays for all MPCs at time t_i and t_{i+1} . The $|\cdot|$ is the absolute value.

In the proposed MCD-based tracking algorithm, three specific thresholds are defined: the matching threshold ϵ_m , filtering threshold ϵ_f , and handover threshold ϵ_h . The ϵ_m is used to match two MPCs based on the similarity of multipaths, i.e., MCD. The ϵ_f is used to filter out sudden multipaths, which may be caused by clutters. The ϵ_h is used to hand over non-successive multipaths that are closely spaced in both time and delay domains (distinguished as ϵ_{h_t} and ϵ_{h_d}), resulting from actual measurements and being unavoidable. The proposed MCD-based tracking algorithm is described as follows:

- An MCD matrix \mathbf{D} , meaning similarity between any S-MPC at time t_i and any S-MPC at time t_{i+1} , is calculated with dimension $L(t_i) \times L(t_{i+1})$.
- A unique S-MPC ID is assigned to match the same S-MPC, which is determined based on conditions as follows:

$$\begin{cases} \mathbf{D}_{u,v} \leq \epsilon_m \\ u = \arg \min_u (\mathbf{D}_{u \in L(t_i), v}) \\ v = \arg \min_v (\mathbf{D}_{u, v \in L(t_{i+1})}) \end{cases} \quad (9)$$

If equation (9) is satisfied, the u th S-MPC at time t_i and the v th S-MPC at time t_{i+1} are considered to be the same S-MPC. Repeat this step to examine all S-MPCs at time t_i and time t_{i+1} .

- Repeat steps 1 and 2 to calculate MCD between any S-MPC at time t_{i+1} and any S-MPC at time t_{i+2} , and obtain new S-MPC IDs. If the w th S-MPC at time t_{i+2} is found to match the v th S-MPC at time t_{i+1} , the w th S-MPC at time t_{i+2} inherits the S-MPC ID from the v th S-MPC at time t_{i+1} , and so forth, obtaining S-MPC IDs for the whole measurements.
- Sudden multipaths are filtered out based on filtering threshold ϵ_f . If the length of S-MPC is less than ϵ_f , this multipath is removed from the set of S-MPCs.
- Hand over S-MPCs that are close to each other. If the time between S-MPCs l_u and l_v is less than ϵ_{h_t} , and the delay between S-MPCs l_u and l_v is less than ϵ_{h_d} , the S-MPC l_u inherits the S-MPC ID from the S-MPC l_v . Repeat this step to hand over all potential S-MPCs.

Through the preceding algorithm, all S-MPCs are extracted and tracked over time, allowing the lifetime and evolution of each S-MPC to be obtained. Based on manual validation, we set $\epsilon_m = 0.3$, $\epsilon_f = 4$, $\epsilon_{h_t} = 5$ and $\epsilon_{h_d} = 10$, respectively. 574, 2885, and 1625 S-MPCs are extracted for the front, left, and right directions, respectively. This indicates that the number of S-MPCs is the highest for the left, while it is the least for the front, which is consistent with the observation from Fig. 4.

An example plot of S-MPC tracking results is shown in Fig. 6, including raw PDPs, S-MPCs results after sensing threshold and S-MPCs results after filtering and handover, respectively. Different color means different extracted S-MPCs in Fig. 6(b) and (c). It can be observed that effective sensing multipaths in raw PDPs are tracked well and reasonably based on S-MPC tracking results, and most of the clutter is eliminated. Besides, S-MPCs with similar time and delay characteristics are clustered, which needs to be considered in the following dynamic modeling approach.

2) *Lifetime*: Lifetime is the duration of existence for S-MPC, measured from the first observed snapshot to the last observed snapshot. Based on the tracking results, we model the distribution of all S-MPCs in different directions. Fig.7 shows the cumulative density function (CDF) fit to the measurements, and the log-normal distribution are plotted for comparison. Although variations in the scatterers distribution and environmental characteristics, the lifetime of S-MPCs

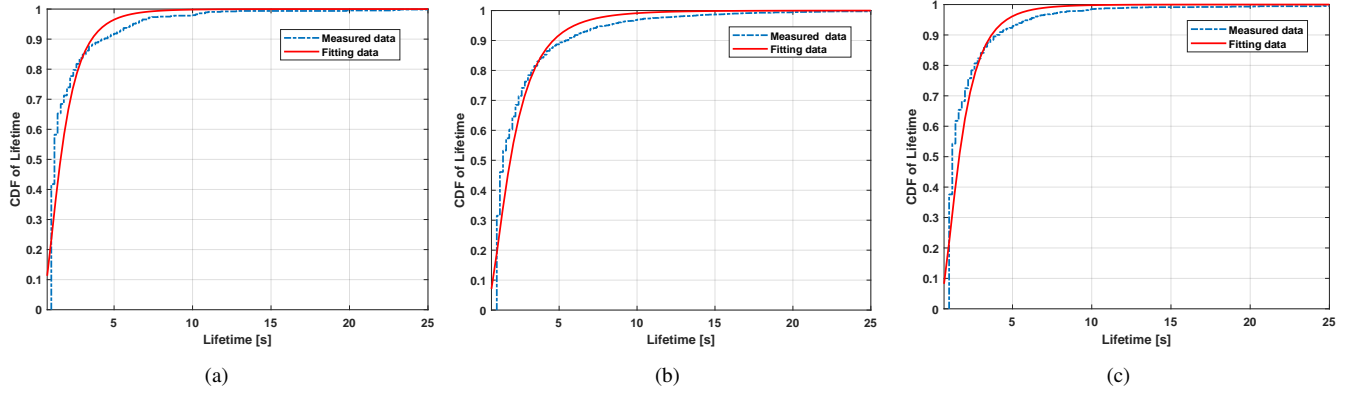


Fig. 7. CDFs of lifetimes. (a) Front. (b) Left. (c) Right.

 TABLE II
 NEW S-MPCs NUMBER PROBABILITY.

New S-MPCs number	0	1	2	3	4	5
Front (%)	96.03	3.47	0.39	0.09	0.01	0.01
Left (%)	82.58	14.84	2.09	0.33	0.11	0.01
Right (%)	89.42	9.07	1.22	0.23	0.05	0.01

in different directions are generally consistent, with 90% of lifetimes falling within 5 seconds. The lifetime in the left is slightly longer than that in other directions, which is caused by noticeable sensing scatters. Finally, we model lifetime as a log-normal distribution with mean value μ_T and standard deviation σ_T as follows, which are summarized in Table IV.

$$f(x|\mu_T, \sigma_T) = \frac{1}{x\sigma_T\sqrt{2\pi}} \exp\left(-\frac{(\ln x - \mu_T)^2}{2\sigma_T^2}\right) \quad (10)$$

3) *Number of New S-MPCs*: As mentioned in section II, the number of all S-MPCs $L(t_i)$ at time t_i consists of two parts: old S-MPCs that appeared before time t_i , denoted as $L(t_{j,i})$, and new S-MPCs that appeared at time t_i , denoted as $L(t_{i,i})$, where $0 < j < i$. Note that $L(t_{j,i})$ is determined by the total number $L(t_j)$ at time t_j and their lifetimes, therefore, only the number of new S-MPCs at each time instant is needed to model to simulate dynamic channel. Based on the tracking results, we counted the number of new S-MPCs in each snapshot. Due to the discreteness and sparsity of S-MPCs, we do not establish a distribution fitting model for parameters; instead, we adopt their number probabilities as the distribution model, as shown in Table II. It is found that in the majority of snapshots, there are no new S-MPCs appearing (the number of new S-MPCs is zero), especially in front direction, with a 96.03% probability of no new S-MPCs. Besides, not many new S-MPCs appear at a single time instant simultaneously (maximum number of new S-MPCs is five). This indicates that S-MPCs in the vehicular ISAC channel are sparse, and this sparsity is more pronounced in front direction compared to other directions, which is reasonable according to actual measurements.

4) *Initial Power and Delay*: We focus on characterizing the initial power distribution and initial delay position distribution of new S-MPCs. In fact, the power and delay of old S-MPCs can be effectively modeled through the evolution model within

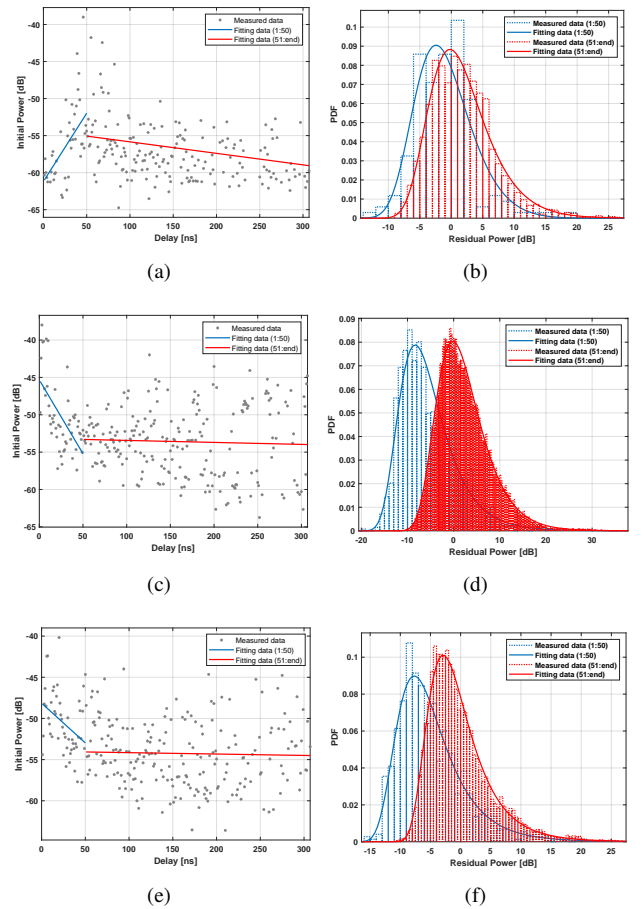


Fig. 8. Initial power in different directions. (a) Dual-slope fitting (Front). (b) Residual power (Front). (c) Dual-slope fitting (Left). (d) Residual power (Left). (e) Dual-slope fitting (Right). (f) Residual power (Right)

lifetime, together with initial power and delay when those old S-MPCs were initially generated.

Generally, power is negatively correlated with delay, i.e., the larger delay, indicating a longer propagation path, the lower power of multipath. Therefore, we model initial power as a dual-slope function of delay, together with a residual power distribution. We set 50 ns as the breakpoint of dual-slope function, because the corresponding sensing distance for 50 ns is

7.5 meters, covering the majority of the driving roads. S-MPCs with delays exceeding 50 ns often originate from scatterers outside the road, such as trees and buildings, and typically have lower power. To have a good fit to measurements, all power is modeled in decibel scale in this paper. Fig. 8(a), (c) and (e) show the initial power in different directions, and the dual-slope functions are plotted for comparison. Note that there is a gap at low delays in front direction from Fig. 4(a), resulting in power being positively correlated with delay in this area. We model initial power as a dual-slope function with parameters p and q , as follows:

$$a_l(t, \tau) = \begin{cases} p_1 \cdot \tau [\text{ns}] + q_1, & 0 \leq \tau < 50 \text{ ns} \\ p_2 \cdot \tau [\text{ns}] + q_2, & 50 \text{ ns} \leq \tau \end{cases} \quad (11)$$

Actually, the relationship between power and delay is not a deterministic function, thus, we also model the residual power distribution. Fig. 8(b), (d) and (e) shows the probability density function (PDF) of residual power. Due to different number of tracked S-MPCs, the number of samples in Fig. 8(d) is higher than others. We model residual power as a Generalized extreme value distribution with shape parameter ξ_r , scale parameter σ_r , and location parameter μ_r , as follows:

$$f(x|\mu_r, \sigma_r, \xi_r) = \frac{1}{\sigma_r} t(x)^{\xi_r+1} e^{-t(x)} \quad (12)$$

where

$$t(x) = \left[1 + \xi_r \left(\frac{x - \mu_r}{\sigma_r} \right) \right]^{-\frac{1}{\xi_r}} \quad (13)$$

Finally, the initial power of S-MPCs is obtained by adding the residual power to delay-based power. The specific fitting values are summarized in Table IV.

Fig. 9 shows the CDF of initial delay of S-MPCs in different directions, and the Gamma distributions are plotted for comparison. It can be observed that the initial delay in front direction has a wider range compared to other directions. For instance, the initial delay of 50% of S-MPCs in front direction can reach to 100 ns, whereas in the left and right directions, it is less than 50 ns. This is consistent with the characteristics mentioned in Section III(B), which demonstrate a large dynamic range of S-MPCs in the delay domain. We model initial delay as a Gamma distribution with the shape parameter α_d and the scale parameter β_d , as follows:

$$f(x|\alpha_d, \beta_d) = \frac{\beta_d^{\alpha_d} x^{\alpha_d-1} e^{-\beta_d x}}{\Gamma(\alpha_d)} \quad (14)$$

where $\Gamma(\cdot)$ is the Gamma function. The specific fitting values are summarized in Table IV.

5) *Evolution Over Successive Time*: In this subsection, we model variations of power and delay of each S-MPCs within its lifetime. Since the initial power and delay of S-MPCs have been modeled, it is only necessary to model the distribution of variations over time to characterize dynamic evolution within lifetime. In our processing, we found that the majority of snapshots exhibit unchanged S-MPCs in the delay domain. Therefore, we consider using a threshold to determine whether delays of S-MPCs undergo dynamic evolution, denoted as k_d . Fig. 10 shows the CDF of variations of delay and power over

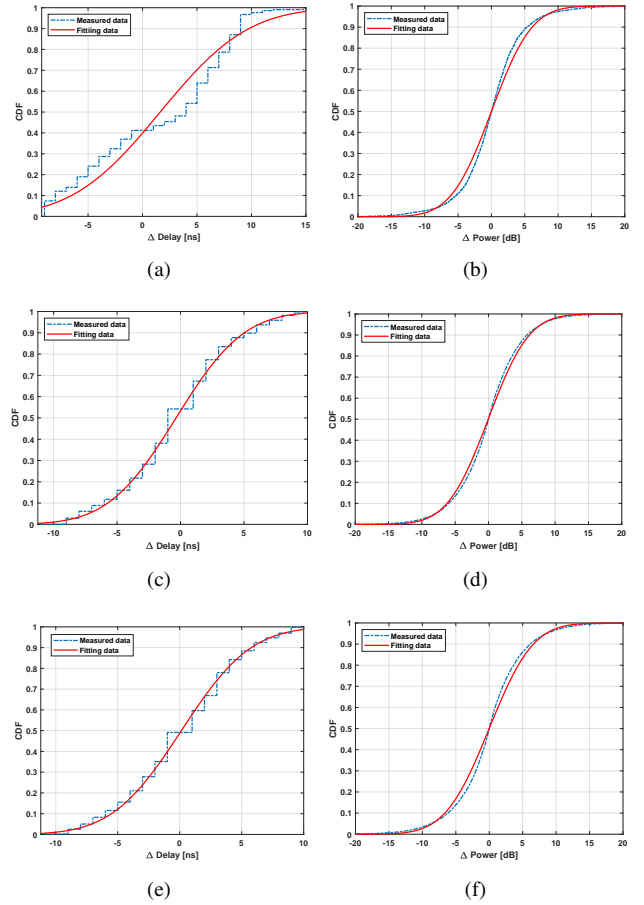


Fig. 9. Evolution over successive time. (a) Delay evolution (Front). (b) Power evolution (Front). (c) Delay evolution (Left). (d) Power evolution (Left). (e) Delay evolution (Right). (f) Power evolution (Right).

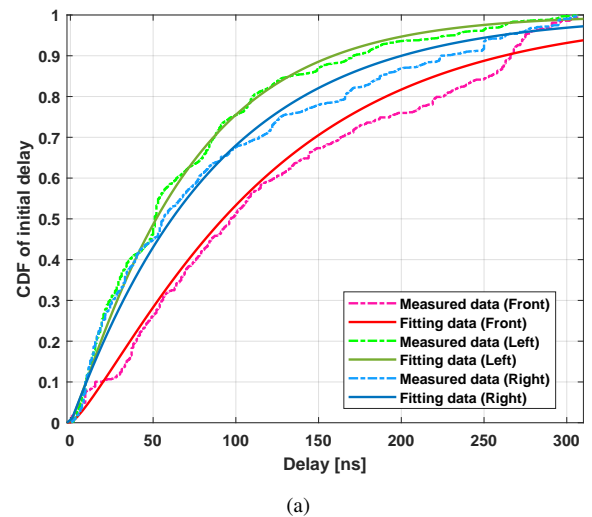


Fig. 10. CDFs of initial delay in different directions.

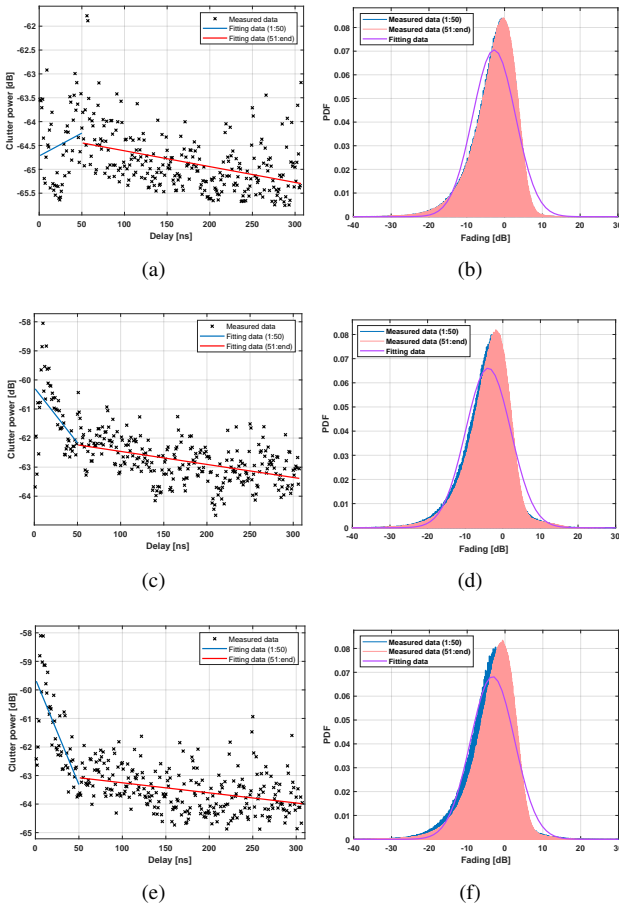


Fig. 11. Clutter power in different directions. (a) Dual-slope fitting (Front). (b) Fading (Front). (c) Dual-slope fitting (Left). (d) Fading (Left). (e) Dual-slope fitting (Right). (f) Fading (Right)

successive time, and the Normal distributions are plotted for comparison. For powers, there is almost no difference among the three directions. For delays, there is a larger variation in front direction, consistent with the observation from Fig. 4, where multipaths exhibit a large dynamic range in the delay domain. We model evolution over successive time as a Normal distribution with the mean value μ_e and standard deviation σ_e , as follows, which are summarized in Table IV.

$$f(x|\mu_e, \sigma_e) = \frac{1}{\sigma_e \sqrt{2\pi}} \exp\left(-\frac{(x - \mu_e)^2}{2\sigma_e^2}\right) \quad (15)$$

6) *Clustering*: Lots of channel measurements have shown that MPCs are generally distributed in groups (clusters), which is suitable for vehicular ISAC channels. Based on the tracking results, we counted the number of S-MPCs within a cluster in each snapshot. Similar to the number of new S-MPCs, we consider probabilities of different numbers as the distribution model, as illustrated in Table III, rather than establishing a distribution fitting model. It can be observed that in more than 90% of clusters in any directions, the number of S-MPCs within a cluster does not exceed 4. For any newly generated S-MPCs, they tend to cluster with other S-MPCs before being assigned across other delay positions. Specifically, determine whether the surroundings of the currently existing S-MPCs

TABLE III
NUMBER OF S-MPCs WITHIN A CLUSTER.

Number	1	2	3	4	5	6	7
Front (%)	35.99	35.75	11.92	6.91	4.22	2.21	0.95
Left (%)	28.73	43.21	16.35	6.88	2.87	1.12	0.41
Right (%)	31.67	40.53	14.54	6.83	3.18	0.50	0.38

satisfy the expected number. If they do not, the new S-MPC is adjustably assigned to be around the currently existing ones.

C. C-MPCs Modeling

Since C-MPCs are randomly distributed across the entire delay domain and lack dynamic characteristics such as lifetime, time evolution, clustering and so on, we mainly focus on characterizing the power distribution for C-MPCs modeling. Similar to the initial power of S-MPCs, power of C-MPCs is negatively correlated with delay, and we model clutter power decay as a dual-slope function of delay, together with a small-scale fading power distribution. In order to keep consistency, 50 ns is still considered as the breakpoint of dual-slope function. Fig. 11(a), (c) and (e) show the clutter power decay in different directions, and the dual-slope functions are plotted for comparison. Compared to initial power of S-MPCs, clutter power is lower and exhibits a smaller range of variation. The fitting model is similar to equation (11), where parameters are replaced by a and b . Fig. 11(b), (d) and (e) shows the PDF of small-scale fading of C-MPCs, which exhibits random variations in delay domain. It can be observed that the distribution of fading in [0-50] ns is similar to that of [50-end] ns in any directions. Therefore, we no longer segment the fading into two parts for modeling. Besides, in order to mitigate the impact of extreme C-MPCs, we model fading as a normal distribution with the mean value μ_c and standard deviation σ_c , consistent with equation (15).

V. MODEL IMPLEMENTATION

A. Implementation

In this subsection, we summarize statistic parameters mentioned before as Table IV, and summarize model implementation steps as Fig.12. First, input the simulation time T and snapshot sampling rate r to determine the total number of simulation snapshots K , and specify the sensing directions. Different sensing directions adopt different channel statistical parameters. Then, initialize the number of S-MPCs in the channel and assign each S-MPC with its lifetime, initial power, and initial delay based on fitted statistical distributions. At the next time step, discard dead S-MPCs based on their lifetime, while counting the remaining number of S-MPCs N_t and the number of multipaths N_s within cluster. Note that if the remaining S-MPCs are zero, indicating that all old S-MPCs have disappeared, reinitialize them; otherwise, evolve the remaining S-MPCs over time, including updating their power and delay according to the fitted functions, then generate new S-MPCs based on the distribution model, including their number, initial power, and initial delay, and perform clustering. Iterate through the above steps repeatedly until the simulation time is met.

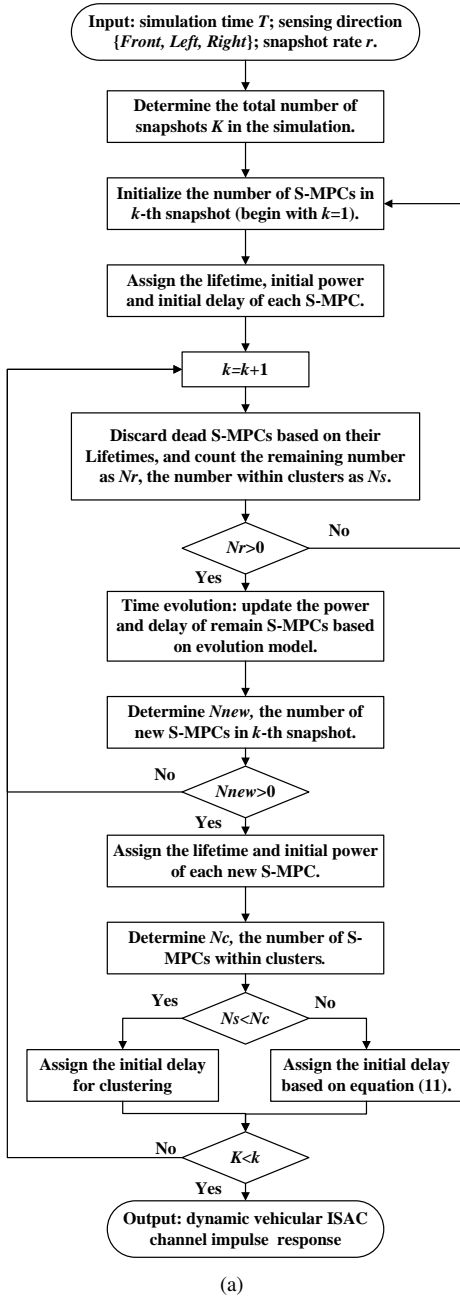


Fig. 12. Flowchart of implementation steps.

Through iteratively repeating the model generation steps, we can obtain dynamically evolving vehicular ISAC channels that extend infinitely along time.

B. Validation

With the proposed model, a dynamic channel impulse responses (CIR) over successive time can be generated for vehicular ISAC channels. We generate CIRs for the duration of 1200 s in three directions. Considering the complexity of the model, the average running time for generating CIR of 1s is approximately 0.026 s (in MATLAB 2022, with 64 GB RAM and Core-i5 CPU), which shows that the model has very low complexity of simulation. To further validate the model,

TABLE IV
THE SUMMARY OF STATISTIC PARAMETERS FOR DYNAMIC VEHICULAR ISAC CHANNELS.

Modeling		Parameter	Front	Left	Right	
Lifetime [s]		μ_T	2.751	2.925	2.795	
		σ_T	0.632	0.708	0.631	
New number		see as Table II				
S-MPCs	Initial power [dB]	[0-50] ns	p	0.184	-0.197	-0.097
			q	-61.191	-45.342	-48.142
			ξ_r	-0.112	0.025	0.067
		[51-end] ns	σ_r	4.089	4.667	4.103
			μ_r	-2.908	-8.231	-7.421
			p	-0.015	-0.002	-0.002
	Initial delay [ns]	q	-55.071	-53.371	-54.073	
		ξ_r	0.135	0.121	0.105	
		σ_r	3.299	3.848	3.772	
		μ_r	-3.294	-4.021	-3.463	
		Power evolution [dB]	α_d	1.311	1.141	1.028
			β_d	81.621	62.431	85.083
Delay evolution [ns]	μ_p	0.001	-0.034	-0.032		
	σ_p	0.747	0.864	0.947		
Number within cluster	[0-50] ns	k_d	0.039	0.028	0.025	
		μ_d	1.625	-0.354	0.132	
	[51-end] ns	σ_d	6.361	4.203	4.403	
		see as Table III				
C-MPCs	Power decay [dB]	a	0.009	-0.038	-0.074	
		b	-64.72	-60.27	-59.62	
	Fading [dB]	a	-0.003	-0.004	-0.004	
		b	-64.28	-62.01	-62.9	
	μ_c	-2.764	-3.88	-3.28		
	σ_c	5.654	6.035	5.846		

second-order statistics, i.e., the root-mean-square delay spread (RMSDS) is employed. Fig. 13 shows the CDF comparisons of RMSDS between measured and simulated ISAC channels in different directions. It can be observed that the simulation is fairly close to the measurements for both front, left and right directions. Note that the simulated CDFs tend to be slightly wider than the measured ones. A possible explanation is that the specific locations of scatterers are not taken into account in simulation, resulting in a more generalized RMSDS range. Overall, the simulated ISAC channel based on the proposed model can reflect the dynamic characteristics of actual channel well, and the research on dynamic ISAC channel models can be the foundation for vehicular ISAC system design and performance evaluation.

VI. CONCLUSION

In this paper, a dynamic statistical channel model is proposed for vehicular ISAC scenarios, which is composed of S-MPCs and C-MPCs. With actual vehicular ISAC channel measurements at 28 GHz, this paper uses a MCD-based tracking algorithm to identify S-MPCs and C-MPCs, and analyzes time-varying sensing characteristics of front, left, and right directions in complicated traffic scenarios. To model the dynamic evolution process, number of new S-MPCs, lifetimes, initial power and delay positions, dynamic variations within their lifetimes, clustering, power decay and fading of C-MPCs are statistically characterized, which are fitted to the best theoretical distributions. In addition, this paper shows the implementation of dynamic model, and validates the model by comparing key statistics of simulations with measurements. The proposed model can generate dynamic behaviors of MPCs in vehicular ISAC scenarios and can be used for vehicular ISAC system design and performance evaluation.

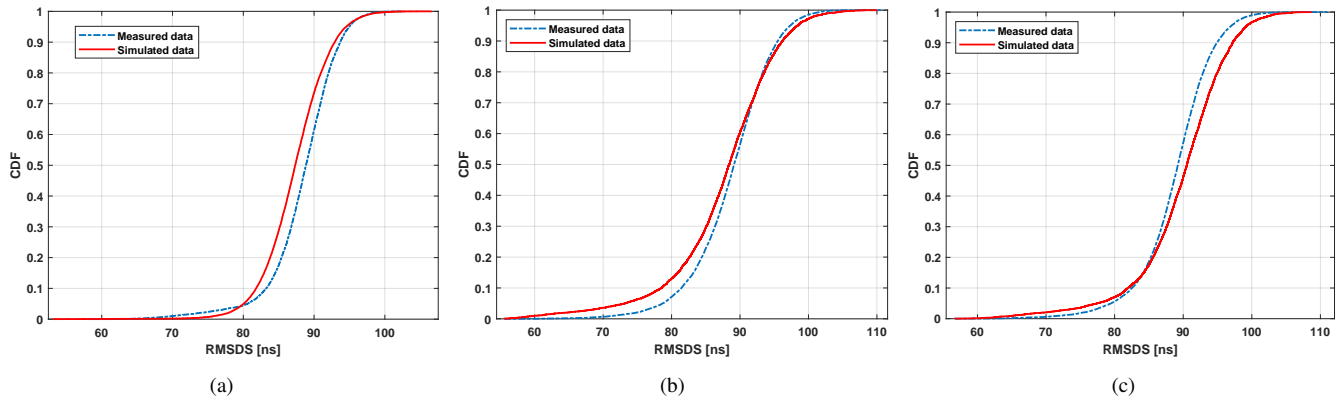


Fig. 13. RMSDS between measured and simulated ISAC channels. (a) Front. (b) Left. (c) Right.

REFERENCES

- [1] L. U. Khan, W. Saad, D. Niyato, Z. Han, and C. S. Hong, "Digital-Twin-Enabled 6G: Vision, Architectural Trends, and Future Directions," *IEEE Communications Magazine*, vol. 60, no. 1, pp. 74–80, 2022.
- [2] U. Demirhan and A. Alkhateeb, "Integrated Sensing and Communication for 6G: Ten Key Machine Learning Roles," *IEEE Communications Magazine*, vol. 61, no. 5, pp. 113–119, 2023.
- [3] Z. Wei, F. Liu, C. Masouros, N. Su, and A. P. Petropulu, "Toward Multi-Functional 6G Wireless Networks: Integrating Sensing, Communication, and Security," *IEEE Communications Magazine*, vol. 60, no. 4, pp. 65–71, 2022.
- [4] Y. Cui, F. Liu, X. Jing, and J. Mu, "Integrating Sensing and Communications for Ubiquitous IoT: Applications, Trends, and Challenges," *IEEE Network*, vol. 35, no. 5, pp. 158–167, 2021.
- [5] X. Cheng, D. Duan, S. Gao, and L. Yang, "Integrated Sensing and Communications (ISAC) for Vehicular Communication Networks (VCN)," *IEEE Internet of Things Journal*, vol. 9, no. 23, pp. 23 441–23 451, 2022.
- [6] C. Chen, W. Chenyu, C. Li, X. Ming, and P. Qingqi, "A V2V Emergent Message Dissemination Scheme for 6G-Oriented Vehicular Networks," *Chinese Journal of Electronics*, vol. 32, no. 6, pp. 1179–1191, 2023.
- [7] X. Meng, F. Liu, C. Masouros, W. Yuan, Q. Zhang, and Z. Feng, "Vehicular Connectivity on Complex Trajectories: Roadway-Geometry Aware ISAC Beam-Tracking," *IEEE Transactions on Wireless Communications*, vol. 22, no. 11, pp. 7408–7423, 2023.
- [8] T. Luettel, M. Himmelsbach, and H.-J. Wuensche, "Autonomous Ground Vehicles—Concepts and a Path to the Future," *Proceedings of the IEEE*, vol. 100, no. Special Centennial Issue, pp. 1831–1839, 2012.
- [9] Q. Liu, R. Luo, H. Liang, and Q. Liu, "Energy-Efficient Joint Computation Offloading and Resource Allocation Strategy for ISAC-Aided 6G V2X Networks," *IEEE Transactions on Green Communications and Networking*, vol. 7, no. 1, pp. 413–423, 2023.
- [10] L. Xujie, T. Jing, X. Yuan, and S. Ying, "Mobility-Aware Multi-Task Migration and Offloading Scheme for Internet of Vehicles," *Chinese Journal of Electronics*, vol. 32, no. 6, pp. 1192–1202, 2023.
- [11] J. Mu, Y. Gong, F. Zhang, Y. Cui, F. Zheng, and X. Jing, "Integrated Sensing and Communication-Enabled Predictive Beamforming with Deep Learning in Vehicular Networks," *IEEE Communications Letters*, vol. 25, no. 10, pp. 3301–3304, 2021.
- [12] D. Cong, S. Guo, S. Dang, and H. Zhang, "Vehicular Behavior-Aware Beamforming Design for Integrated Sensing and Communication Systems," *IEEE Transactions on Intelligent Transportation Systems*, vol. 24, no. 6, pp. 5923–5935, 2023.
- [13] C. Huang, R. He, B. Ai, A. F. Molisch, B. K. Lau, K. Haneda, B. Liu, C.-X. Wang, M. Yang, C. Oestges, and Z. Zhong, "Artificial Intelligence Enabled Radio Propagation for Communications—Part II: Scenario Identification and Channel Modeling," *IEEE Transactions on Antennas and Propagation*, vol. 70, no. 6, pp. 3955–3969, 2022.
- [14] R. He, C. Schneider, B. Ai, G. Wang, Z. Zhong, D. A. Dupleich, R. S. Thomae, M. Boban, J. Luo, and Y. Zhang, "Propagation Channels of 5G Millimeter-Wave Vehicle-to-Vehicle Communications: Recent Advances and Future Challenges," *IEEE Vehicular Technology Magazine*, vol. 15, no. 1, pp. 16–26, 2020.
- [15] L. Xiong, Z. Zhang, and D. Yao, "Dynamic Doppler Prediction in High-speed Rail using Long Short-Term Memory Neural Network," *Transactions on Emerging Telecommunications Technologies*, vol. 32, no. 9, p. e4269, 2021.
- [16] J. Zhang, J. Wang, Y. Zhang, Y. Liu, Z. Chai, G. Liu, and T. Jiang, "Integrated Sensing and Communication Channel: Measurements, Characteristics, and Modeling," *IEEE Communications Magazine*, pp. 1–7, 2023.
- [17] Z. Zhang, R. He, B. Ai, M. Yang, C. Li, H. Mi, and Z. Zhang, "A General Channel Model for Integrated Sensing and Communication Scenarios," *IEEE Communications Magazine*, vol. 61, no. 5, pp. 68–74, 2023.
- [18] R. He, B. Ai, G. Wang, M. Yang, C. Huang, and Z. Zhong, "Wireless Channel Sparsity: Measurement, Analysis, and Exploitation in Estimation," *IEEE Wireless Communications*, vol. 28, no. 4, pp. 113–119, 2021.
- [19] J. Karedal, F. Tufvesson, N. Czink, A. Paier, C. Dumard, T. Zemen, C. F. Mecklenbrauker, and A. F. Molisch, "A Geometry-based Stochastic MIMO Model for Vehicle-to-vehicle Communications," *IEEE Transactions on Wireless Communications*, vol. 8, no. 7, pp. 3646–3657, 2009.
- [20] X. Zhang, R. He, M. Yang, B. Ai, S. Wang, W. Li, W. Sun, L. Li, P. Huang, and Y. Xue, "Measurements and Modeling of Large-Scale Channel Characteristics in Subway Tunnels at 1.8 and 5.8 GHz," *IEEE Antennas and Wireless Propagation Letters*, vol. 22, no. 3, pp. 561–565, 2023.
- [21] J. Yu, W. Chen, F. Li, C. Li, K. Wang, K. Yang, and F. Chang, "Measurement-based V2V radio channel analysis and modelling for bridge scenarios at 5.9 GHz," *IET Communications*, vol. 14, no. 3, pp. 376–386, 2020. [Online]. Available: <https://ietresearch.onlinelibrary.wiley.com/doi/abs/10.1049/iet-com.2018.6274>
- [22] R. He, A. F. Molisch, F. Tufvesson, Z. Zhong, B. Ai, and T. Zhang, "Vehicle-to-Vehicle Propagation Models With Large Vehicle Obstructions," *IEEE Transactions on Intelligent Transportation Systems*, vol. 15, no. 5, pp. 2237–2248, 2014.
- [23] Z. Su, L. Liu, J. Zhang, Y. Fan, K. Wang, L. Zhuang, Z. Wang, and S. Zheng, "Analysis of Channel Non-Stationarity for V2V and V2I Communications at 5.9GHz in Urban Scenarios," in *2022 IEEE International Conference on Communications Workshops (ICC Workshops)*, 2022, pp. 1130–1134.
- [24] R. He, O. Renaudin, V.-M. Kolmonen, K. Haneda, Z. Zhong, B. Ai, and C. Oestges, "A Dynamic Wideband Directional Channel Model for Vehicle-to-Vehicle Communications," *IEEE Transactions on Industrial Electronics*, vol. 62, no. 12, pp. 7870–7882, 2015.
- [25] M. Yang, B. Ai, R. He, Z. Ma, H. Mi, D. Fei, Z. Zhong, Y. Li, and J. Li, "Dynamic V2V Channel Measurement and Modeling at Street Intersection Scenarios," *IEEE Transactions on Antennas and Propagation*, vol. 71, no. 5, pp. 4417–4432, 2023.
- [26] R. He, B. Ai, G. L. Stüber, G. Wang, and Z. Zhong, "Geometrical-Based Modeling for Millimeter-Wave MIMO Mobile-to-Mobile Channels," *IEEE Transactions on Vehicular Technology*, vol. 67, no. 4, pp. 2848–2863, 2018.
- [27] J. Wang, J. Zhang, Y. Zhang, T. Jiang, L. Yu, and G. Liu, "Empirical Analysis of Sensing Channel Characteristics and Environment Effects at 28 GHz," in *2022 IEEE Globecom Workshops (GC Wkshps)*, 2022, pp. 1323–1328.
- [28] Z. Zhang, R. He, M. Yang, C. Li, X. Zhang, C. Wang, Y. Yuan, B. Ai, and Z. Zhong, "Millimeter Wave Channel Measurements and Analysis

- for Integrated Sensing and Communication Scenario,” in *2023 IEEE International Symposium on Antennas and Propagation and USNC-URSI Radio Science Meeting (USNC-URSI)*, 2023, pp. 415–416.
- [29] Z. Zhang, R. He, B. Ai, M. Yang, X. Zhang, R. Chen, H. Zhang, and Z. Zhong, “A Shared Multipath Components Evolution Model for Integrated Sensing and Communication Channels,” *IEEE Antennas and Wireless Propagation Letters*, vol. 22, no. 12, pp. 2975–2978, 2023.
- [30] A. Ali, N. Gonzalez-Prelcic, R. W. Heath, and A. Ghosh, “Leveraging Sensing at the Infrastructure for mmWave Communication,” *IEEE Communications Magazine*, vol. 58, no. 7, pp. 84–89, 2020.
- [31] Y. Liu, J. Zhang, Y. Zhang, Z. Yuan, and G. Liu, “A Shared Cluster-based Stochastic Channel Model for Integrated Sensing and Communication Systems,” *IEEE Transactions on Vehicular Technology*, pp. 1–13, 2023.
- [32] P. Kumari, J. Choi, N. González-Prelcic, and R. W. Heath, “IEEE 802.11ad-Based Radar: An Approach to Joint Vehicular Communication-Radar System,” *IEEE Transactions on Vehicular Technology*, vol. 67, no. 4, pp. 3012–3027, 2018.
- [33] Y. Chen, Z. Yu, J. He, J. Li, and G. Wang, “A Scatterer-based Hybrid Channel Model for Integrated Sensing and Communications (ISAC),” in *2023 IEEE 34th Annual International Symposium on Personal, Indoor and Mobile Radio Communications (PIMRC)*, 2023, pp. 1–7.
- [34] R. Yang, C.-X. Wang, J. Huang, E.-H. M. Aggoune, and Y. Hao, “A Novel 6G ISAC Channel Model Combining Forward and Backward Scattering,” *IEEE Transactions on Wireless Communications*, vol. 22, no. 11, pp. 8050–8065, 2023.
- [35] J. Lou, R. Liu, C. Jiang, X. Han, Z. Han, Q. Yang, and Z. Wang, “A Unified Channel Model for Both Communication and Sensing in Integrated Sensing and Communication Systems,” in *2023 IEEE 98th Vehicular Technology Conference (VTC2023-Fall)*, 2023, pp. 1–6.